

Diverse and Admissible Trajectory Forecasting through Multimodal Context Understanding

Seong Hyeon Park¹, Gyubok Lee², Manoj Bhat³, Jimin Seo⁴, Minseok Kang⁵,
Jonathan Francis^{3,6}, Ashwin Jadhav³, Paul Pu Liang³, and
Louis-Philippe Morency³

¹ Hanyang University, Seoul, Korea
shpark@spa.hanyang.ac.kr

² Yonsei University, Seoul, Korea
glee48@yonsei.ac.kr

³ Carnegie Mellon University, Pittsburgh, PA, USA
{mbhat, jmf1, arjadhav, pli, morency}@cs.cmu.edu

⁴ Korea University, Seoul, Korea
jmseo0607@korea.ac.kr

⁵ Sogang University, Seoul, Korea
ahstarwab@sogang.ac.kr

⁶ Bosch Research Pittsburgh, Pittsburgh, PA, USA

Abstract. Multi-agent trajectory forecasting in autonomous driving requires an agent to accurately anticipate the behaviors of the surrounding vehicles and pedestrians, for safe and reliable decision-making. Due to partial observability over the goals, contexts, and interactions of agents in these dynamical scenes, directly obtaining the posterior distribution over future agent trajectories remains a challenging problem. In realistic embodied environments, each agent’s future trajectories should be *diverse* since multiple plausible sequences of actions can be used to reach its intended goals, and they should be *admissible* since they must obey physical constraints and stay in drivable areas. In this paper, we propose a model that fully synthesizes multiple input signals from the multimodal world—the environment’s scene context and interactions between multiple surrounding agents—to best model all diverse and admissible trajectories. We offer new metrics to evaluate the diversity of trajectory predictions, while ensuring admissibility of each trajectory. Based on our new metrics as well as those used in prior work, we compare our model with strong baselines and ablations across two datasets and show a **35%** performance-improvement over the state-of-the-art.

Keywords: Trajectory Forecasting, Diversity, Generative Modeling, Autonomous Driving, Datasets

1 Introduction

Trajectory forecasting is an important problem in autonomous driving scenarios, where an autonomous vehicle must anticipate the behavior of other surrounding agents (e.g., vehicles and pedestrians), within a dynamically-changing environment, in order to plan its own actions accordingly. However, since none of the goals, contexts, or interactions are directly observed, predicting future trajectories is a challenging problem [27, 34, 39]. It necessitates both the estimation of

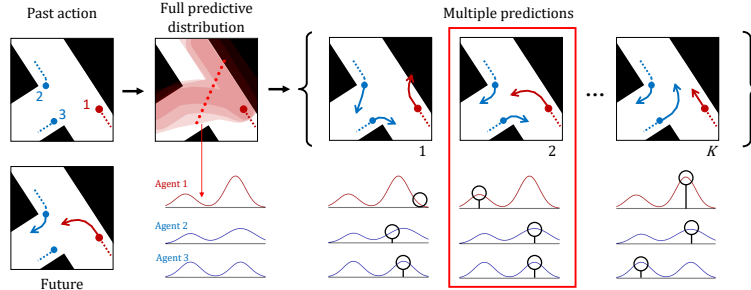


Fig. 1. Diverse and admissible trajectory forecasting. Based on the existing context, there can be multiple valid hypothetical futures. Therefore, the predicted future trajectory distribution should have multiple modes representing multiple plausible goals (*diversity*) while at the same time assigning low density to the implausible trajectories that either conflict with the other agents or are outside valid drivable areas (*admissibility*).

plausible agent actions based on observable environmental features (e.g., road structures, agent interactions) as well as the simulation of agents’ hypothetical future trajectories toward their intended goals. In realistic embodied environments, there are multiple plausible sequences of actions that an agent can take to reach its intended goals. However, each trajectory must obey physical constraints (e.g., Newton’s laws) and stay in the statistically plausible locations in the environment (i.e., the drivable areas). In this paper, we refer to these attributes as *diverse* and *admissible* trajectories, respectively, and illustrate some examples in Fig. 1. Achieving diverse and admissible trajectory forecasting for autonomous driving allows each agent to make the best predictions, by taking into account all valid actions that other agents could take. In addition, it allows each agent to assess the surrounding situation to ensure safety and prevent accidents.

To predict a diverse set of admissible trajectories, each agent must understand its *multimodal* environment, consisting of the scene context as well as interactions between multiple surrounding agents. While the scene context gives direct information about regions an agent can drive in, observation of other agents’ trajectories can provide additional environmental context. For example, conceptual constraints over the agent’s motion (e.g., traffic laws, road etiquette) may be inferred from the motion of the surrounding agents. Therefore, the model’s ability to extract and meaningfully represent multimodal cues is crucial.

Concurrently, another challenging aspect of trajectory forecasting lies in encouraging models to make diverse predictions about future trajectories. However, due to high-costs in data collection, most public datasets are not explicitly annotated for multiple future trajectories [8, 18, 21]. Vanilla predictive models that fit future trajectories based only on the existing annotations would severely underestimate the diversity of all possible trajectories. In addition, measuring the quality of predictions using existing annotation-based measures (e.g., displacement errors [29]) does not faithfully score diverse and admissible trajectory predictions.

As a step towards multimodal understanding for diverse trajectory forecasting, our contribution is *four-fold*.

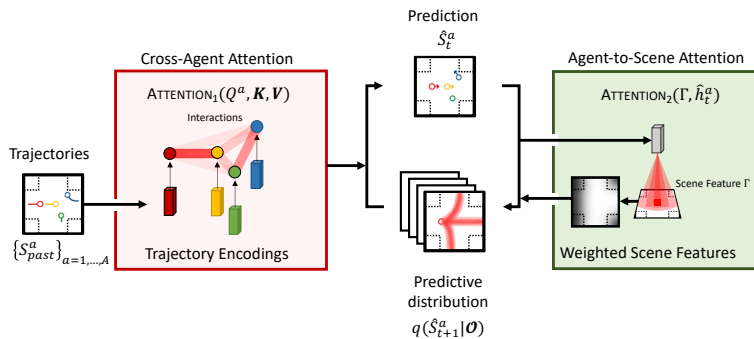


Fig. 2. Overview of our multimodal attention approach. Best viewed in color. The cross-agent attention module (left) generates an attention map, based on the encoded trajectories of nearby agents. The agent-to-scene attention model (right) generates an attention map over the scene, based on the posterior approximations.

1. We propose a model that addresses the lack of diversity and admissibility for trajectory forecasting through the understanding of the multimodal environmental context. As illustrated in Fig. 2, our approach explicitly models agent-to-agent and agent-to-scene interactions through “self-attention” [35] among multiple agent trajectory encodings, and a conditional trajectory-aware “visual attention” [38] over the map, respectively. Together with a constrained flow-based decoding trained with symmetric cross-entropy [26], this allows our model to generate diverse and admissible trajectory candidates by fully integrating all environmental contexts.
2. We propose a new approximation of the true trajectory distribution based on a differentiable drivable-area map. This approximation is used when evaluating our posterior likelihood. Previous approximation methods [26] utilize ground-truth (GT) trajectories to model the real distribution. However, only one GT annotation is available per agent. Our approximation method does not rely on GT samples and empirically facilitates greater diversity in the predicted trajectories while ensuring admissibility.
3. We propose a new metric, Drivable Area Occupancy (DAO), to evaluate the diversity of the trajectory predictions while ensuring admissibility. This new metric utilizes the drivable-area map, without requiring multiple annotations of trajectory futures. We couple this new metric with standard metrics from prior art, such as Average Displacement Error (ADE) and Final Displacement Error (FDE), to compare our model with existing baselines.
4. We provide a programmatic set of procedures to convert the NUSCENES [6] tracking data to a new dataset for trajectory forecasting. The procedure includes trajectory association, smoothing, imputation, and generation of the drivable-area features. These features are used for approximation of the real trajectory distribution and for calculating our new metrics. We set new state-of-the-art performance for multi-agent trajectory forecasting, wherein our model enjoys a **35%** performance-improvement over the current baselines.

We will publish tools to replicate our data and results which we hope will advance the study of diverse trajectory forecasting.

2 Related Work

Multimodal trajectory forecasting requires a detailed understanding of the agent’s environment. Many works integrate information from multiple modalities [20, 23], such as RGB image and LiDAR point-cloud information to model the surrounding environment [19, 26] and high dimensional map data to modeling vehicle lane segmentation [3, 7, 39]. Other methods additionally fuse different combinations of map context [3, 7, 10], LiDAR [19], and RGB [21, 28] with the intention of jointly capturing all interactions between the agents and environment [1, 14, 30]. Without mechanisms to explicitly model agent-to-agent and agent-to-scene interactions, we hypothesize that these models are unable to capture complex nonlinear interactions in the high-dimensional input space. In this paper, we study and propose methods to explicitly model these interactions, escalating performance in trajectory forecasting.

Multi-agent modeling aims to learn representations that summarize the behavior of one agent given its surrounding agents. These interactions are often modeled through either spatial-oriented methods or through neural attention-based methods. Spatial-oriented methods use pooling approaches across individual agent representations [9, 19, 39] and usually take into account inter-agent distances, through a relative coordinate system [3, 15, 22, 27]. Despite their wide usage, spatial-oriented methods are designed to concentrate only on adjacent (spatially close) agents and assume a fixed number of agents in the scene; they also limit the maximum number of agents. Attention-based methods use attention [35] architectures to model multi-agent interaction for applications involving pedestrians [12, 30, 36], sports players [11, 32], indoor robots [24], and vehicle trajectories [21, 34]. In this paper, we use a cross-agent attention module to model the agent-to-agent interaction. Rather than using this information solely for prediction, we additionally generate attended scene context, conditioned on these cross-agent representations. We hypothesize that the attended map context will lead to improved tractability in modeling high-dimensional correlations in the scene. We support this with our empirical results in Section 6.

Diverse trajectory prediction: Many models follow a deterministic trajectory-prediction approach [9, 39] and, therefore, struggle to estimate the diversity in the future trajectories. Some works have applied generative models such as Generative Adversarial Networks (GANs) [13, 14, 30, 39] and Variational Auto Encoders (VAEs) [19] to encourage diverse predictions. However, these approaches focus more on generating and scoring multiple output candidates and focus less on analyzing the diversity across distributional modes.

Trajectory forecasting: Trajectory forecasting has been studied in various domains, spanning marine vessels, aircraft, satellites, motor vehicles, and pedestrians [2, 5, 14, 27, 31]. Tasks involving motor vehicles and pedestrians are especially challenging, due to the high stochasticity that arises from attempting to model complex latent factors (e.g., human intent, “social” agent interacts, and scene context) [8]. Despite some promising empirical results, it remains difficult to evaluate both the diversity and admissibility of predictions. In this paper, we define the task of diverse and admissible trajectory forecasting and provide a new dataset generated from NUSCENES [6], a popular image tracking source. We also define new task metrics that specifically assess models on the basis of prediction

diversity and admissibility, and we analyze model generalization based on data from multiple domains.

3 Problem Formulation

3.1 Model Architecture

We define the terminology that constitutes our problem. An *agent* is a dynamic on-road object that is represented as a sequence of 2D coordinates, i.e., a spatial position over time. We denote the position for agent a at time t as $S_t^a \in \mathbb{R}^2$. By writing $S_{t_1:t_2}^a$, we represent the sequence of its positions, between t_1 and t_2 . \mathbf{S}^a (bold) to denote full sequence of positions for agent a . We set $t = 0$ as *present*, $t \leq 0$ as *past*, and $t > 0$ as *prediction* or simply, *pred*. We often split the sequence into two parts, with respect to the *past* and *pred* sub-sequences: we denote these as \mathbf{S}_{past}^a and \mathbf{S}_{pred}^a , respectively. A *scene* is a high-dimensional structured data that describes the present environmental context around the agent. For this, we utilize a bird’s eye view array, denoted $\Phi \in \mathbb{R}^{H \times W \times C}$, where H and W are the sizes of field around the agent and C is the channel size of the scene, where each channel consists of distinct information such as the drivable area, position, and distance encodings.

Combining the *scene* and all *agent* trajectories yields an *episode*. In an episode \mathcal{X} , there is a variable A number of agents, each of which plays for different time periods from between the variable *start time* t_s^a and *final time* t_f^a . As a result, the episode is the set $\{\mathbf{S}^1, \mathbf{S}^2, \dots, \mathbf{S}^A, \Phi\}$ where $\mathbf{S}^a \equiv S_{t_s^a:t_f^a}^a$. In the combined setting, we often use bold $\mathbf{S} \equiv \{\mathbf{S}^1, \mathbf{S}^2, \dots, \mathbf{S}^A\}$ to denote the agents subset of the episode \mathcal{X} and write \mathbf{S}_{past} or \mathbf{S}_{pred} to represent the set of past or pred segments of A agents. Since \mathbf{S}_{past} and Φ serve as the observed information cue used for the prediction, they are often called *observation* simply being denoted as $\mathcal{O} \equiv \{\mathbf{S}_{past}, \Phi\}$. Finally, we may add the subscript $n = 1, 2, \dots, N$ to all the notations, such as $\mathcal{X}_n, \mathcal{O}_n, \Phi_n, S_{t,n}^a, S_{t_1:t_2,n}^a, \mathbf{S}_n^a$, or \mathbf{S}_n to distinguish the information from different episodes.

We define *diversity* to be the level of coverage in a model’s predictions, across modes in a distribution representing all possible future trajectories. We denote the model distribution as $q(\mathbf{S}_{pred}|\mathcal{O})$ and want the model to generate K candidates or *hypotheses*, denoted as $\hat{\mathbf{S}}_{pred} \equiv \{\hat{\mathbf{S}}_{pred}^1, \hat{\mathbf{S}}_{pred}^2, \dots, \hat{\mathbf{S}}_{pred}^K\}$. We interpret $\hat{\mathbf{S}}_{pred}$ as a set of independent hypotheses that might have happened, given the same *observation*. Instead of generating samples from one mode, which we refer to as *perturbation*, we expect to build a model that generates multiple hypotheses that cover multiple modes.

Finally, we acknowledge that encouraging a model’s predictions to be diverse, alone, is not sufficient for accurate and safe output; the model predictions should lie in the support of the real future trajectory distribution p , i.e., predictions should be *admissible*. Given the observation \mathcal{O} , it is futile to predict samples around regions that are physically and statistically implausible to reach. In conclusion, our task is *diverse and admissible multi-agent motion forecasting* by modeling multiple modes in the posterior distribution over the *pred* trajectories, given the observation: $p(\mathbf{S}_{pred}|\mathcal{O})$.

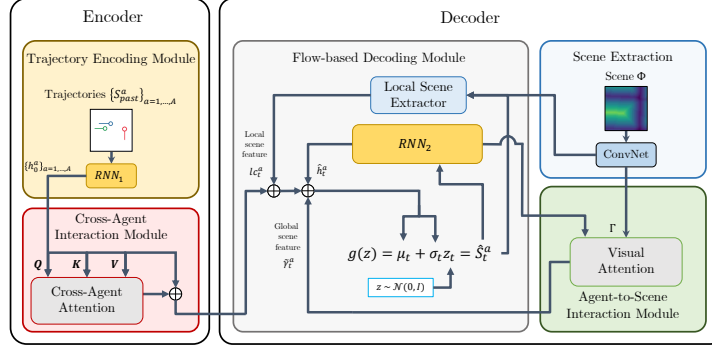


Fig. 3. Model Architecture. The model consists of an encoder-decoder architecture: the encoder takes as past agent trajectories and calculates cross-agent attention, and the flow-based decoder predicts future trajectories by attending scene contexts for each decoding step.

4 Proposed Approach

We hypothesize that future trajectories of human drivers should follow distributions of multiple modes conditioned on the scene context and social behaviors of agents. Therefore, we design our model to explicitly capture both agent-to-scene interactions and cross-agent interactions with respect to each agent of interest. Through our objective function, we explicitly encourage the model to learn a distribution with multiple modes by taking into account past trajectories and attended scene context.

As illustrated in Fig. 3, our model consists of an encoder-decoder architecture. The encoder has two modules to capture cross-agent interactions and existing trajectories. The decoder has three modules: the local scene extractor, the agent-to-scene interaction module, and the flow-based decoding module. Please refer to Fig. 4 for a detailed illustration of our main proposed modules.

The *encoder* extracts past trajectory encoding for each agent, then calculates and fuses the interaction features among the agents. Given a set of past trajectories \mathbf{S}_{past} in an observation \mathcal{O} , we encode each agent’s past trajectory $S_{past}^a \in \mathbf{S}_{past}$ by feeding it to the agent trajectory encoding module. The module utilizes a recurrent neural network (RNN) to summarize the past trajectory. It iterates through the past trajectory with Eq. (1) and its final output h_0^a (at *present* $t = 0$) is utilized as the agent embedding. Collecting the embeddings for all agents, we get $\mathbf{h}_0 \equiv \{h_0^1, h_0^2, \dots, h_0^A\}$. We then pass \mathbf{h}_0 to the cross-agent interaction module, depicted in Fig. 4(a), which uses *self-attention* [35] to generate a cross-agent representation. We linearly transform each agent embedding to get a query-key-value triple, (Q^a, K^a, V^a) . Next, we calculate the interaction features through self-attention with $\text{ATTENTION}_1(Q^a, \mathbf{K}, \mathbf{V})$, where $\mathbf{K}, \mathbf{V} \equiv \{K^1, \dots, K^A\}, \{V^1, \dots, V^A\}$. Finally, the fused agent encoding $\tilde{\mathbf{h}} \equiv \{\tilde{h}^1, \tilde{h}^2, \dots, \tilde{h}^A\}$ is calculated by adding the features to each agent embedding (see Eq. (2) and Fig. 4(b)). The architectural details of the encoder, which include the parameters for the agent encoding RNN and the

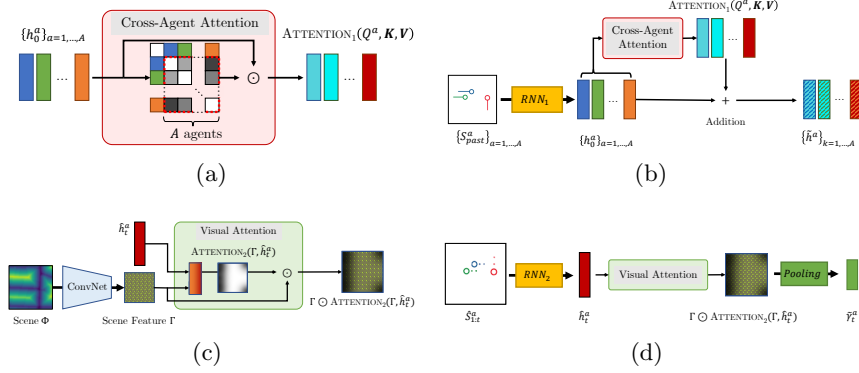


Fig. 4. (a) Cross-agent attention. Interaction between each agent is modeled using attention, (b) Cross-agent interaction module. Agent trajectory encodings are corrected via cross-agent attention. (c) Visual attention. Agent-specific scene features are calculated using attention. (d) Agent-to-scene interaction module. Pooled vectors are retrieved from pooling layer after visual attention.

cross-agent attention structures, are given in the supplemental material.

$$h_t^a = \text{RNN}_1(S_{t-1}^a, h_{t-1}^a) \quad (1)$$

$$\tilde{h}^a = h_0^a + \text{ATTENTION}_1(Q^a, \mathbf{K}, \mathbf{V}) \quad (2)$$

The *decoder* takes the final encodings $\tilde{\mathbf{h}}$ and the scene context Φ as inputs. We first extract the scene feature through a *ConvNet*, $\Gamma = \text{CNN}(\Phi)$. The decoder then autoregressively generates the future position \hat{S}_t^a , while referring to both the local scene context γ_t^a and the global scene context $\tilde{\gamma}_t^a$ from the agent-to-scene interaction module. The local scene feature γ_t^a is gathered using bilinear interpolation on 2×2 crop of Γ corresponding to the physical position \hat{S}_{t-1}^a . Then, the feature is concatenated with the encoding \tilde{h}^a and processed through fully-connected layers to make the “local context” lc_t^a . We call this part the local scene extractor. The global scene feature $\tilde{\gamma}_t^a$ is calculated using *visual-attention* [38] to generate weighted scene features, as shown in Fig. 4(c). To calculate the attention, we first make the encoding of the previous outputs $\hat{S}_{1:t-1}^a$, using a RNN in Eq. (3), whose output— \hat{h}_t^a —is used to calculate the pixel-wise attention at each decoding step, for each agent; the global scene feature $\tilde{\gamma}_t^a$ (1D vector) is gathered by pooling (pixel-wise sum) the attended feature map as described in Eq. (4) and Fig. 4(d). Finally, $\tilde{\gamma}_t^a$, \hat{h}_t^a , and lc_t^a are concatenated to make the “global context” gc_t^a in Eq. (5).

$$\hat{h}_t^a = \text{RNN}_2(\hat{S}_{1:t-1}^a, \hat{h}_{t-1}^a) \quad (3)$$

$$\tilde{\gamma}_t^a = \text{POOL}(\Gamma \odot \text{ATTENTION}_2(\hat{h}_t^a, \Gamma)) \quad (4)$$

$$gc_t^a = \text{CONCAT}(\tilde{\gamma}_t^a, \hat{h}_t^a, lc_t^a) \quad (5)$$

The flow-based decoding module generates the future position \hat{S}_t^a . The module utilizes *Normalizing Flow* [25], a generative modeling method based on a bijective

and differentiable mapping. In particular, we choose an autoregressive design [17, 26, 27]. We use fully-connected layers to project the global context gc_t^a down to a 6-dimensional vector, and we split it into a vector $\hat{\mu}_t \in \mathbb{R}^2$ and a matrix $\hat{\sigma}_t \in \mathbb{R}^{2 \times 2}$. Next, we transform a standard Gaussian sample $z_t \sim \mathcal{N}(\mathbf{0}, I) \in \mathbb{R}^2$, by the bijective and differentiable mapping $g(z_t; \mu_t, \sigma_t) = \sigma_t \cdot z_t + \mu_t = \hat{S}_t^a$. The “hats” in $\hat{\mu}_t$ and $\hat{\sigma}_t$ are removed, in order to note that they went through the following details. To ensure the positive definiteness, we apply matrix exponential $\sigma_t = \text{expm}(\hat{\sigma}_t)$ using the formula in [4]. Also, to improve the the physical *admissibility* of the prediction, we apply the constraint $\mu_t = \hat{S}_{t-1}^a + \alpha(\hat{S}_{t-1}^a - \hat{S}_{t-2}^a) + \hat{\mu}_t$, where α is a model degradation coefficient. When $\alpha = 1$, the constraint is equivalent to *Verlet integration* [37], used in some previous works [26, 27], which gives the a perfect constant velocity (CV) prior to the model. However, we found empirically that, the model easily overfits to the dataset when the the perfect CV prior is used, and perturbing the CV prior model with α prevents overfitting. We use $\alpha = 0.5$ in our model and an analysis on the effect of the degradation coefficient α is given in the supplemental material.

Iterating the autoregressive decoding procedure, we get the future trajectory prediction \hat{S}_{pred}^a for each agent. Note that by sampling multiple instances of z_{pred} , we can generate the multiple future $\hat{S}_{\text{pred}}^{k,a}$.

4.1 Drivable Area Map and Approximating \mathbf{P}

In this work, we generate a binary mask feature of size $\mathbb{R}^{H \times W}$ that denotes the drivable spaces around the agents. We call the feature *drivable area map* and utilize it for three different purposes: 1) deriving the approximated true trajectory distribution \tilde{p} , 2) calculating the diversity and admissibility measures, and 3) building the scene context input Φ for the model.

Particularly, \tilde{p} is a key component for the evaluation of $H(q, p)$ in our training objective, Eq. (7). Since $H(q, p)$ penalizes the predicted trajectories with respect to the real distribution, the approximation should not underestimate some region of the real distribution, or diversity in the prediction could be erroneously penalized. Previous works on deriving \tilde{p} utilized the ground-truth (GT) trajectories to model the true distribution p [26]. However, there is often only one GT annotation available in datasets and the approximation based on the GT might severely assign low probability around some region in p . To cope with such problem in the previous methods, we propose a new method to derive \tilde{p} using the drivable area. Our \tilde{p} is defined based on the assumptions that every location on the drivable-area is equally probable for future trajectories to appear in and that the locations on non-drivable area are increasingly less probable, proportional to the distance from the drivable area. To derive it, we first apply the distance transform on the drivable area map, to encode the distance on each non-drivable location. Lastly, we apply softmax over the entire map to constitute it as a probability distribution. The visualizations of the \tilde{p} are available in Fig. 7. Procedures regarding the diversity and admissibility measure will be discussed in Section 5.3; details on deriving \tilde{p} and the scene context input Φ , as well as additional visualizations and qualitative results, are given in the supplemental material.

4.2 Learning

Our model learns to predict the joint distribution over the future trajectories of the agents present in a given episode. In detail, we focus on predicting the conditional distribution $p(\mathbf{S}_{\text{pred}}|\mathcal{O})$ where the future trajectory \mathbf{S}_{pred} depends on the set of observations of the past trajectories and the scene context $\mathcal{O} \equiv \{\mathbf{S}_{\text{past}}, \Phi\}$ given an episode. As described in the previous sections, our model utilizes a bijective and differentiable mapping, parameterized by a learnable parameter θ , $S_{\text{pred}}^a = g_\theta(z \sim q_0; \mathcal{O})$ between the future trajectory and a Gaussian prior q_0 to generate and evaluate the future trajectory. Such technique, commonly aliased ‘normalizing flow’, enables our model not only to generate multiple candidate samples of future, but also to evaluate the ground-truth trajectory according to the predicted distribution q_θ by using the change-of-variable formula in Eq. (6).

$$q_\theta(S_{\text{pred}}^a|\mathcal{O}) = q_0(g^{-1}(S_{\text{pred}}^a)) \left| \det(\partial S_{\text{pred}}^a / \partial(g^{-1}(S_{\text{pred}}^a)) \right|^{-1} \quad (6)$$

As a result, our model can simply learn to close the discrepancy between the predicting distribution q_θ and the real world distribution p . In particular, we choose to minimize the combination of forward and reverse cross-entropy $H(p, q)$ and $H(q, p)$, also known as ‘symmetric cross-entropy’, between the two distributions in Eq. (7) by optimizing our model parameter θ . Minimizing symmetric cross-entropy allows model to learn generating diverse and plausible trajectory, which is mainly used in [26].

$$\min_{\theta} H(p, q_\theta) + \beta H(q_\theta, p) \quad (7)$$

To realize this, we gather the ground-truth trajectories \mathbf{S} and scene context Φ from the dataset \mathcal{D} that we assume to well reflect the real distribution p , then optimize the model parameter θ such that 1) the density of the ground-truth future trajectories on top of the predicted distribution q_θ is maximized and 2) the density of the predicted samples on top of the real distribution p is also maximized as described in Eq.(8).

$$\min_{\theta} \mathbb{E}_{\mathbf{S}, \Phi \sim \mathcal{D}} \left[\mathbb{E}_{S_{\text{pred}}^a \in \mathbf{S}} - \log q_\theta(S_{\text{pred}}^a|\mathcal{O}) + \beta \mathbb{E}_{\hat{S}_{\text{pred}}^a \sim q_\theta} - \log p(\hat{S}_{\text{pred}}^a|\mathcal{O}) \right] \quad (8)$$

Such symmetric combination of the two cross-entropy guides our model to predict q_θ that covers all plausible modes in the future trajectory while penalizing the bad samples that are less likely under the real distribution p . However, one major problem inherent in this setting is that we cannot actually evaluate p in practice. To cope with the problem, several ways of approximating p by using a separate model \tilde{p} have been suggested so far [26]. In this paper, we propose a new way of modeling \tilde{p} which approximates p using a discrete grid map derived from the differentiable drivable area map in our dataset which considers every drivable region around the ego-vehicle to be equally probable that the future trajectories are placed. The details about our new \tilde{p} is included in the supplemental material. Applying bilinear interpolation around each prediction time-step in the generative sample \hat{S}_{pred}^a , we get the evaluation $\tilde{p}(\hat{S}_{\text{pred}}^a|\mathcal{O})$ that is differentiable with respect to the model parameter θ . Our overall loss function is:

$$\frac{1}{\sum_{n=1}^N A(n)} \sum_{n=1}^N \sum_{a=1}^{A(n)} \left[-\log q_\theta(S_{\text{pred},n}^a|\mathcal{O}_n) + \beta \frac{1}{K} \sum_{k=1}^K -\log p(\hat{S}_{\text{pred},n}^{a,k}|\mathcal{O}_n) \right], \quad (9)$$

where N is the batch size, $A(n)$ is the number of total agents in n th episode, and K is the number of candidates to sample per agent. Since this objective is fully differentiable with respect to the model parameter θ , we train our model using Adam optimizer [16], a popular variant of the stochastic gradient descent algorithm. We also use adaptive learning rate scheduling and early stopping. Optimization details are included in the supplementary.

5 Experimental Setup

The primary goal in the following experiments is to evaluate our model, baselines, and ablations on the following criteria- 1. Leveraging mechanisms that explicitly model agent-to-agent and agent-to-scene interactions (experiment 1 and 2). 2. Producing diverse trajectory predictions, while obeying admissibility constraints on the trajectory candidates given different approximation methods for the true trajectory distribution p (experiment 3). 3. Remaining robust to an increasing number of agents in the scene (agent complexity; experiment 4). 4. Generalizing to other domains (experiment 5). We implement all models in PyTorch trained on NVIDIA TITAN X GPUs. Procedural, architectural, and training details are included in the supplementary material.

5.1 Dataset

Most current autonomous driving trajectory forecasting datasets are insufficient for evaluating predictions, due to the small size and the limited number of multimodal cues [21].

The ARGOVERSE motion forecasting dataset consists of a large volume of forecasting data with drivable area annotations, but lacks certain modalities i.e LiDAR point-clouds and map images. We have generated motion forecasting datasets from NUSCENES and ARGOVERSE tracking dataset using their original annotations through programmatic trajectory association, smoothing, and imputation. Unlike the ARGOVERSE forecasting dataset, this new dataset provides additional context information from LiDAR point-clouds and map information, for better forecasting performance. We utilize the trajectory record, vectorized geometry, and drivable area annotation as modalities for our research. In order to make the experimental setup of NUSCENES similar to ARGOVERSE, we crop each sequence to be 5 seconds long in total; 3 seconds for prediction and 2 seconds for observation, with a sampling rate of 2 Hz. Background information relating to NUSCENES, ARGOVERSE trajectory data generation are included in the supplementary material. By evaluating baselines and our models on both real world datasets, we provide complementary validation of each model’s diversity, admissibility, and generalizability across domains. Data extraction procedures and quantitative results on the simulated data are discussed in the supplementary material.

5.2 Baseline Models

Deterministic baselines: We compare three deterministic models with our approach, to examine our model’s ability to capture agent-to-agent interaction: *LSTM-based encoder-decoder* [33] (LSTM), *convolutional social pooling LSTM* (CSP) [9], and a deterministic version of *multi-agent tensor fusion* (MATF-D) [39]. For our deterministic model, we use an LSTM with our cross-agent

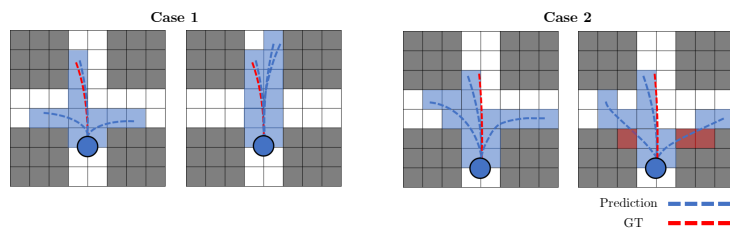


Fig. 5. We motivate the need for multiple metrics, to assess diversity and admissibility. Case 1: DAO measures are equal, even though predictions have differing regard for the modes in the posterior distribution. Case 2: RF measures are equal, despite differing regard for the cost of leaving the drivable area. In both cases, it is important to distinguish between conditions—we do this by using DAO, RF, and DAC together.

attention module in the encoder, which we refer to as the *cross-agent attention model* (CAM). Because each model is predicated on an LSTM component, we set the capacity to be the same in all cases, to ensure fair comparison.

Stochastic baselines: We experiment three stochastic baselines. Our first stochastic baseline is a model based on a Variational Autoencoder structure, DESIRE [19], which utilizes scene contexts and an iterative refinement process. The second baseline model is a Generative Adversarial Network version of MATF-GAN [39]. Our third baseline is the Reparameterized Pushforward Policy (R2P2-MA) [27] which is a modified version of R2P2 [26] for multi-agent prediction. To validate our model’s ability to extract scene information and generate diverse trajectories, multiple versions of our models are tested. While these models can be used as stand-alone models to predict diverse trajectories, comparison amongst these new models is equivalent to an ablation study of our final model. CAM-NF is a CAM model with a flow-based decoder. LOCAL-CAM-NF is CAM-NF with local scene features. GLOBAL-CAM-NF is LOCAL-CAM-NF with global scene features. Finally, ATTGLOBAL-CAM-NF is GLOBAL-CAM-NF with agent-to-scene attention, which is our main proposed model.

5.3 Metrics

Measuring diversity and admissibility: We define multiple metrics that provide a thorough interpretation about the behavior of each model in terms of precision, diversity, and admissibility. For the i -th trajectory, we first evaluate a prediction in terms of Euclidean errors: *average displacement error* $\text{ADE}^{(i)} = \frac{1}{T} \sum_{t=1}^T \|S_t^i - \hat{S}_t^i\|_2$ and *final displacement error* $\text{FDE}^{(i)} = \|S_{t_f}^i - \hat{S}_{t_f}^i\|_2$, or **ERROR** to denote both. To evaluate N predictions (i.e., precision), we use the average and the minimum **ERRORS**: $\text{AVGERROR} = \frac{1}{N} \sum_{i=1}^N \text{ERROR}^{(i)}$ and $\text{MINERROR} = \min\{\text{ERROR}^{(1)}, \dots, \text{ERROR}^{(N)}\}$. A large **AVGERROR** implies that predictions are spread out, and a small **MINERROR** implies at least one of predictions has high precision. From this observation, we define new evaluation metrics that capture diversity in predictions: the ratio of **AVGADE** to **MINADE** and **AVGFDE** to **MINFDE**, namely **RA** and **RF**. In particular, **RF** is robust to the variability of magnitude in velocity in predictions because high **AVGADE** and high **MINADE** caused by large magnitudes will be offset and only the directional variability will remain. As a result, **RF** provides a handy tool that can distinguish between



Fig. 6. Metric quality spectrum. Our newly proposed metrics: RF measures the spread of predictions in Euclidean distance, DAO measures diversity in predictions that are only admissible. DAC measures extreme off-road predictions that defy admissibility.

predictions with multiple modes (diversity) and predictions with a single mode (perturbation). For deterministic models, RA and RF have a value of 1.

$$\text{Ratio of AVGFDE to MINFDE (RF)} = \frac{\text{AVGFDE}}{\text{MINFDE}} \quad (10)$$

$$\text{Drivable Area Occupancy (DAO)} = \frac{\text{count}(\text{traj}_{\text{pix}})}{\text{count}(\text{driv}_{\text{pix}})} \quad (11)$$

We also report performance on additional metrics that are designed to capture diversity and admissibility in predictions. We follow [8] in the use of *Drivable Area Count* (DAC), $\text{DAC} = \frac{n-m}{n}$, where m is the number of predictions that go out of the drivable area and n is the total number of predictions. Next, we propose a new metric, *Drivable Area Occupancy* (DAO), which measures the percentage of pixels that predicted trajectories occupy in the drivable area. Shown in Eq. (11), $\text{count}(\text{traj}_{\text{pix}})$ is the number of pixels occupied by predictions and $\text{count}(\text{driv}_{\text{pix}})$ is the total number of pixels of the drivable area, both within a pre-defined grid around the ego-vehicle. Due to the nature of DAO and DAC, the number of trajectory hypotheses should be set equally for fair comparison of models.

We use RF, DAO, and DAC to assess the diversity and admissibility of models. Initially, DAO may seem like a reasonable standalone measure of both diversity and admissibility, as it only cares about diversity in a reasonable region of interest. However, DAO itself cannot distinguish between *diversity* (Section 3) and arbitrary stochasticity in predictions, as illustrated by Case 1 in Fig. 5: although DAO measures of both predictions are equal, the causality behind each prediction is different and we must distinguish the two. RF and DAO work in a complementary way and we, therefore, use both for measuring diversity. To assure the *admissibility* of predictions, we use DAC which explicitly counts off-road predictions, as shown by Case 2 in Fig. 5. As a result, assessing predictions using DAO along with RF and DAC provides a holistic view of the quantity and the quality of diversity in predictions; the characteristics of each metric is summarized in Fig. 6.

For our experiments, we use MINADE and MINFDE to measure *precision*, and use RF, DAC, and DAO to measure both *diversity* and *admissibility*. Due to the nature of DAO, where the denominator in our case is the number of overlapping pixels in a 224×224 grid, we normalize it by multiplying by 10,000 when reporting results. For the multi-agent experiment (experiment 4), relative improvement (RI) is calculated as we are interested in the relative improvement as the number of agents increases. If not specified, the number of hypotheses are set to 12 and MINFDE is reported for the performance.

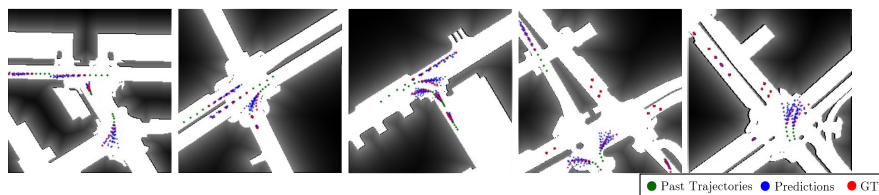


Fig. 7. Our map loss and corresponding model predictions. Each pixel on our map loss denotes probability of future trajectories; higher probability values are represented by brighter pixels. Our approach generates diverse and admissible future trajectories. More visualizations of qualitative results are provided in the supplementary material.

6 Results and Discussion

In this section, we show experimental results on numerous settings including the comparison with the baseline, and ablation studies of our model. We first show the effect of our cross-agent interaction module and agent-to-scene interaction module on the model performance, then we analyze the performance with respect to different numbers of agents, and other datasets. All experiments are measured with MINADE, MINFDE, RF, DAC, and DAO for holistic interpretation.

Table 1. Deterministic models on NUSCENES. Our proposed model outperforms the existing baselines.

Model	MINADE (\downarrow)	MINFDE (\downarrow)
LSTM	1.186	2.408
CSP [9]	1.390	2.676
MATF-D [39]	1.261	2.538
CAM (OURS)	1.124	2.318

Table 2. Stochastic models on NUSCENES. **: unstable outputs observed on R2P2-MA.

Model	MINADE (\downarrow)	MINFDE (\downarrow)	RF (\uparrow)	DAO (\uparrow)	DAC (\uparrow)
DESIRE [19]	0.937	1.808	1.754	9.430	0.376
MATF-GAN [39]	1.053	2.124	1.194	5.950	0.391
R2P2-MA [26]	1.185	2.215	1.611	13.50**	0.396
CAM-NF (OURS)	0.756	1.386	2.113	11.70	0.400
LOCAL-CAM-NF (OURS)	0.772	1.404	2.066	11.70	0.400
GLOBAL-CAM-NF (OURS)	0.744	1.359	2.103	11.60	0.400
ATTGLOBAL-CAM-NF (OURS)	0.638	1.171	2.558	12.28	0.399

Effectiveness of cross-agent interaction module: We show the performance of one of our proposed models CAM, which utilizes our cross-agent attention module, along with three deterministic baselines as shown in Table 1. For each model we test, agent-to-agent interaction is considered in different ways. CSP models the interaction through layers of convolutional networks, and the interaction is implicitly calculated within the receptive field of convolutional layers. MATF-D is an extension of convolutional social pooling with scene information. CAM explicitly defines the interaction between each agent by using attention. The result shows that CAM outperforms other baselines in both MINADE and MINFDE, indicating that the explicit way of modeling agent-to-agent interaction

Table 3. Optimizing using p loss outperforms MSE loss on NUSCENES.

Model	MINADE (\downarrow)	MINFDE (\downarrow)	rF (\uparrow)	DAO (\uparrow)	DAC (\uparrow)
ATTGLOBAL-CAM-NF(MSE)	0.763	1.390	2.009	12.09	0.400
ATTGLOBAL-CAM-NF	0.638	1.171	2.558	12.28	0.399

Table 4. Multi-agent experiments on NUSCENES (MINFDE). RI denotes ratio of MINFDE for 10 vs. 1 agent. Our approach best models multi-agent interactions.

Model	1 agent	3 agents	5 agents	10 agents	RI(1-10)
LSTM	2.736	2.477	2.442	2.268	17.1%
CSP [9]	2.871	2.679	2.671	2.569	10.5%
DESIRE [19]	2.150	1.846	1.878	1.784	17.0%
MATF GAN [39]	2.377	2.168	2.150	2.011	15.4%
R2P2-MA [26]	2.227	2.135	2.142	2.048	8.0%
ATTGLOBAL-CAM-NF (OURS)	1.278	1.158	1.100	0.964	24.6%

performs better in terms of precision than an implicit way of modeling interaction using convolutional networks used in CSP and MATF-D. Interestingly, CAM outperforms MATF-D that utilizes scene information. This infers that our cross-agent interaction module has the ability to learn the geometric structure of the roads given by the trajectories of surrounding agents.

Effectiveness of agent-to-scene interaction module: The performance of stochastic models is compared in Table 2. We experiment with removing scene processing operations in the decoder to validate the importance of our proposed agent-to-scene interaction module. As mentioned previously, generating multiple modes of sample requires a strong scene processing module and a diversity-oriented decoder. Our proposed models all outperform other stochastic baseline models in terms of precision. MATF-GAN has a small rF inferring that the predictions are mostly unimodal, while other models such as VAE-based model DESIRE and flow-based models R2P2 and OURS show more spread in their predictions. We note that R2P2 was not designed for multi-agent setting which causing it to make unreasonably shaking outputs. Our model has the highest *DAC* and *DAO*, indicating that our models exhibit diverse and admissible predictions by accurately utilizing scene context.

Effectiveness of new p loss: We experiment with MSE and our drivable area-based approximation of p in Table 3. Using our map loss in training shows superior results in most of the reported metrics. In particular, the precision and the diversity of predictions increases drastically as reflected in MINERROR and rF while DAC remains unchanged. Our map loss assures admissibility while improving precision and diversity, as drivable-area associated \tilde{p} provides additional possible regions of future trajectories.

Complexity from number of agents: We experiment with varying number of surrounding agents as shown in Table 4. Throughout all models, the performance increases as the number of agents increases even though we observe that many agents in the surrounding do not move significantly. In terms of relative improvement RI, as calculated between 1 agent and 10 agents, our model has the most improvement, indicating that our model makes the most use of the fine-grained trajectories of surrounding agents to generate future trajectories.

Generalizability across datasets: We further compare our model with baselines extensively across two more real world datasets: NUSCENES and ARGOVERSE

Table 5. Results of baseline models (upper partition) and our proposed model (lower partition). ATTGLOBAL-CAM-NF is our full proposed model and others in the lower partition are the ablations. The metrics are abbreviated as follows: MINADE(**A**), MINFDE(**B**), RF(**C**), DAO(**D**), DAC(**E**). Improvements indicated by arrows. *: larger is better, as long as **A** and **B** are small. **: unstable outputs observed on R2P2-MA.

Model	ARGOVERSE					NUSCENES				
	A (↓)	B (↓)	C (↑)*	D (↑)*	E (↑)*	A (↓)	B (↓)	C (↑)*	D (↑)*	E (↑)*
LSTM	1.441	2.780	1.000	1.786	0.378	1.186	2.408	1.000	1.690	0.391
CSP [9]	1.385	2.567	1.000	1.799	0.379	1.390	2.676	1.000	1.710	0.388
MATF-D [39]	1.344	2.484	1.000	1.768	0.379	1.261	2.538	1.000	1.690	0.384
DESIRE [19]	0.777	1.276	3.642	11.80	0.301	0.937	1.808	1.754	9.430	0.376
MATF-GAN [39]	1.214	2.316	1.099	6.075	0.376	1.053	2.124	1.194	5.950	0.391
R2P2-MA [27]	1.270	2.190	1.589	<u>18.10</u> **	0.381	1.185	2.215	1.611	<u>13.50</u> **	0.396
CAM	1.131	2.504	1.000	1.750	0.389	1.124	2.318	1.000	1.670	0.404
CAM-NF	0.852	1.347	2.763	17.60	0.378	0.756	1.386	2.113	11.70	0.400
LOCAL-CAM-NF	0.807	1.250	2.858	17.00	0.381	0.772	1.404	2.066	11.70	0.400
GLOBAL-CAM-NF	0.807	1.241	3.068	16.90	0.380	0.744	1.359	2.103	11.60	0.400
ATTGLOBAL-CAM-NF	0.731	1.126	3.278	15.50	0.383	0.638	1.171	2.558	12.28	0.399

to test generalization to different environments. We show results in Table 7 where we outperform or achieve comparable results as compared to the baselines. For ARGOVERSE, we additionally outperform MFP3 [34] in MINFDE with 6 hypotheses: our full model shows a MINFDE of 0.915, while MFP3 achieves 1.399.

7 Conclusion

In this paper, we tackled the problem of generating diverse and admissible predictions by understanding each agent’s multimodal context. We proposed a model that learns agent-to-agent interactions and agent-to-scene interactions using attention mechanisms, resulting in better prediction in terms of precision, diversity, and admissibility. We also developed a new approximation method that provides richer information about the true trajectory distribution and allows more accurate training of flow-based generative models. Finally, we present new metrics that provide a holistic view of the quantity and the quality of diversity in prediction, and a NUSCENES trajectory extraction code to support future research in diverse and admissible trajectory forecasting.

References

1. Alahi, A., Goel, K., Ramanathan, V., Robicquet, A., Fei-Fei, L., Savarese, S.: Social lstm: Human trajectory prediction in crowded spaces. In: Proceedings of the IEEE conference on computer vision and pattern recognition. pp. 961–971 (2016)
2. Ayhan, S., Samet, H.: Aircraft trajectory prediction made easy with predictive analytics. In: Proceedings of the 22nd ACM SIGKDD International Conference on Knowledge Discovery and Data Mining. pp. 21–30 (2016)
3. Bansal, M., Krizhevsky, A., Ogale, A.: Chauffeurnet: Learning to drive by imitating the best and synthesizing the worst. arXiv preprint arXiv:1812.03079 (2018)
4. Bernstein, D.S., So, W.: Some explicit formulas for the matrix exponential. IEEE Transactions on Automatic Control **38**(8), 1228–1232 (1993)
5. Borkowski, P.: The ship movement trajectory prediction algorithm using navigational data fusion. Sensors **17**(6), 1432 (2017)

6. Caesar, H., Bankiti, V., Lang, A.H., Vora, S., Liong, V.E., Xu, Q., Krishnan, A., Pan, Y., Baldan, G., Beijbom, O.: nuscenes: A multimodal dataset for autonomous driving. arXiv preprint arXiv:1903.11027 (2019)
7. Casas, S., Luo, W., Urtasun, R.: Intentnet: Learning to predict intention from raw sensor data. In: Conference on Robot Learning. pp. 947–956 (2018)
8. Chang, M.F., Lambert, J., Sangkloy, P., Singh, J., Bak, S., Hartnett, A., Wang, D., Carr, P., Lucey, S., Ramanan, D., et al.: Argoverse: 3d tracking and forecasting with rich maps. In: Proceedings of the IEEE Conference on Computer Vision and Pattern Recognition. pp. 8748–8757 (2019)
9. Deo, N., Trivedi, M.M.: Convolutional social pooling for vehicle trajectory prediction. In: Proceedings of the IEEE Conference on Computer Vision and Pattern Recognition Workshops. pp. 1468–1476 (2018)
10. Djuric, N., Radosavljevic, V., Cui, H., Nguyen, T., Chou, F.C., Lin, T.H., Schneider, J.: Short-term motion prediction of traffic actors for autonomous driving using deep convolutional networks. arXiv preprint arXiv:1808.05819 (2018)
11. Felsen, P., Lucey, P., Ganguly, S.: Where will they go? predicting fine-grained adversarial multi-agent motion using conditional variational autoencoders. In: Proceedings of the European Conference on Computer Vision (ECCV). pp. 732–747 (2018)
12. Fernando, T., Denman, S., Sridharan, S., Fookes, C.: Soft + hardwired attention: An LSTM framework for human trajectory prediction and abnormal event detection. CoRR **abs/1702.05552** (2017), <http://arxiv.org/abs/1702.05552>
13. Goodfellow, I., Pouget-Abadie, J., Mirza, M., Xu, B., Warde-Farley, D., Ozair, S., Courville, A., Bengio, Y.: Generative adversarial nets. In: Advances in neural information processing systems. pp. 2672–2680 (2014)
14. Gupta, A., Johnson, J., Fei-Fei, L., Savarese, S., Alahi, A.: Social gan: Socially acceptable trajectories with generative adversarial networks. In: Proceedings of the IEEE Conference on Computer Vision and Pattern Recognition. pp. 2255–2264 (2018)
15. Kim, B., Kang, C.M., Kim, J., Lee, S.H., Chung, C.C., Choi, J.W.: Probabilistic vehicle trajectory prediction over occupancy grid map via recurrent neural network. In: 2017 IEEE 20th International Conference on Intelligent Transportation Systems (ITSC). pp. 399–404. IEEE (2017)
16. Kingma, D.P., Ba, J.: Adam: A method for stochastic optimization. arXiv preprint arXiv:1412.6980 (2014)
17. Kingma, D.P., Salimans, T., Jozefowicz, R., Chen, X., Sutskever, I., Welling, M.: Improved variational inference with inverse autoregressive flow. In: Advances in neural information processing systems. pp. 4743–4751 (2016)
18. Krajewski, R., Bock, J., Kloeker, L., Eckstein, L.: The highd dataset: A drone dataset of naturalistic vehicle trajectories on german highways for validation of highly automated driving systems. In: 2018 21st International Conference on Intelligent Transportation Systems (ITSC). pp. 2118–2125. IEEE (2018)
19. Lee, N., Choi, W., Vernaza, P., Choy, C.B., Torr, P.H., Chandraker, M.: Desire: Distant future prediction in dynamic scenes with interacting agents. In: Proceedings of the IEEE Conference on Computer Vision and Pattern Recognition. pp. 336–345 (2017)
20. Liang, P.P., Lim, Y.C., Tsai, Y.H.H., Salakhutdinov, R., Morency, L.P.: Strong and simple baselines for multimodal utterance embeddings. In: Proceedings of the 2019 Conference of the North American Chapter of the Association for Computational Linguistics: Human Language Technologies, Volume 1 (Long and Short Papers) (2019)
21. Ma, Y., Zhu, X., Zhang, S., Yang, R., Wang, W., Manocha, D.: Trafficpredict: Trajectory prediction for heterogeneous traffic-agents. In: Proceedings of the AAAI Conference on Artificial Intelligence. vol. 33, pp. 6120–6127 (2019)

22. Park, S.H., Kim, B., Kang, C.M., Chung, C.C., Choi, J.W.: Sequence-to-sequence prediction of vehicle trajectory via lstm encoder-decoder architecture. In: 2018 IEEE Intelligent Vehicles Symposium (IV). pp. 1672–1678. IEEE (2018)
23. Pham, H., Liang, P.P., Manzini, T., Morency, L., Póczos, B.: Found in translation: Learning robust joint representations by cyclic translations between modalities. In: The Thirty-Third AAAI Conference on Artificial Intelligence, AAAI 2019 (2019)
24. Qureshi, A.H., Nakamura, Y., Yoshikawa, Y., Ishiguro, H.: Show, attend and interact: Perceivable human-robot social interaction through neural attention q-network. In: 2017 IEEE International Conference on Robotics and Automation (ICRA). pp. 1639–1645. IEEE (2017)
25. Rezende, D.J., Mohamed, S.: Variational inference with normalizing flows. arXiv preprint arXiv:1505.05770 (2015)
26. Rhinehart, N., Kitani, K.M., Vernaza, P.: R2p2: A reparameterized pushforward policy for diverse, precise generative path forecasting. In: Proceedings of the European Conference on Computer Vision (ECCV). pp. 772–788 (2018)
27. Rhinehart, N., McAllister, R., Kitani, K., Levine, S.: Precog: Prediction conditioned on goals in visual multi-agent settings. In: Proceedings of the IEEE International Conference on Computer Vision. pp. 2821–2830 (2019)
28. Rodriguez, C., Fernando, B., Li, H.: Action anticipation by predicting future dynamic images. In: Proceedings of the European Conference on Computer Vision (ECCV). pp. 0–0 (2018)
29. Rudenko, A., Palmieri, L., Herman, M., Kitani, K.M., Gavrila, D.M., Arras, K.O.: Human motion trajectory prediction: A survey. arXiv preprint arXiv:1905.06113 (2019)
30. Sadeghian, A., Kosaraju, V., Sadeghian, A., Hirose, N., Rezatofghi, H., Savarese, S.: Sophie: An attentive gan for predicting paths compliant to social and physical constraints. In: Proceedings of the IEEE Conference on Computer Vision and Pattern Recognition. pp. 1349–1358 (2019)
31. Shapiro, I.I.: The prediction of satellite orbits. In: Dynamics of Satellites/Dynamique des Satellites, pp. 257–312. Springer (1963)
32. Sun, C., Karlsson, P., Wu, J., Tenenbaum, J.B., Murphy, K.: Stochastic prediction of multi-agent interactions from partial observations. arXiv preprint arXiv:1902.09641 (2019)
33. Sutskever, I., Vinyals, O., Le, Q.: Sequence to sequence learning with neural networks. *Advances in Neural Information Processing Systems* **4** (09 2014)
34. Tang, C., Salakhutdinov, R.R.: Multiple futures prediction. In: *Advances in Neural Information Processing Systems*. pp. 15398–15408 (2019)
35. Vaswani, A., Shazeer, N., Parmar, N., Uszkoreit, J., Jones, L., Gomez, A.N., Kaiser, L., Polosukhin, I.: Attention is all you need. In: *Advances in neural information processing systems*. pp. 5998–6008 (2017)
36. Vemula, A., Muelling, K., Oh, J.: Social attention: Modeling attention in human crowds. In: 2018 IEEE international Conference on Robotics and Automation (ICRA). pp. 1–7. IEEE (2018)
37. Verlet, L.: Computer” experiments” on classical fluids. i. thermodynamical properties of lennard-jones molecules. *Physical review* **159**(1), 98 (1967)
38. Xu, K., Ba, J., Kiros, R., Cho, K., Courville, A., Salakhudinov, R., Zemel, R., Bengio, Y.: Show, attend and tell: Neural image caption generation with visual attention. In: *International conference on machine learning*. pp. 2048–2057 (2015)
39. Zhao, T., Xu, Y., Monfort, M., Choi, W., Baker, C., Zhao, Y., Wang, Y., Wu, Y.N.: Multi-agent tensor fusion for contextual trajectory prediction. In: *Proceedings of the IEEE Conference on Computer Vision and Pattern Recognition*. pp. 12126–12134 (2019)

8 Additional Experimental Details

8.1 nuScenes Trajectory Extraction Process

NUSCENES [6] contains 850 different real-world driving records, each of which spans 40 frames (20 seconds) of LiDAR point-cloud data, RGB camera images, ego-vehicle pose records, and 3D bounding-box annotations of the surrounding vehicles, pedestrians, animals, etc. It also provides a map API that gives an access to the drivable area information. Based on this setting, we generate trajectories by associating the bounding boxes of the same agents, using the agent IDs available in the dataset. The resultant sequences, however, include noise and missing points, due to annotation errors and occlusion issues, as depicted in Fig. 8(b). To combat this, we employ *Kalman smoothing* [16] with the constant velocity linear model in Eq. (12), in order to filter the noise and impute missing points. When initializing the Kalman filter, we utilize *Expectation-Maximization* (EM) [1] to fit the initial states and the covariance parameters (transition and emission), with respect to the sequences.

$$\begin{bmatrix} x_{t+1} \\ y_{t+1} \\ z_{t+1} \\ \dot{x}_{t+1} \\ \dot{y}_{t+1} \\ \dot{z}_{t+1} \end{bmatrix} = \begin{bmatrix} 1 & 0 & 0 & 0.5 & 0 & 0 \\ 0 & 1 & 0 & 0 & 0.5 & 0 \\ 0 & 0 & 1 & 0 & 0 & 0.5 \\ 0 & 0 & 0 & 1 & 0 & 0 \\ 0 & 0 & 0 & 0 & 1 & 0 \\ 0 & 0 & 0 & 0 & 0 & 1 \end{bmatrix} \begin{bmatrix} x_t \\ y_t \\ z_t \\ \dot{x}_t \\ \dot{y}_t \\ \dot{z}_t \end{bmatrix} \quad (12)$$

Next, we construct the episodes for our trajectory dataset. The lengths of the past and prediction segments are set to 2 and 3 seconds (4 and 6 frames), respectively. As a result, an individual episode should contain a snippet of length 5 seconds (10 frames) from the smoothed trajectory, with a maximum of 30 samples extracted from one episode. For each snippet, we normalize the coordinate system, such that the ego-pose at the present time (4th frame) is placed at the origin (0, 0).

For each episode, we generate the road mask of dimension 224×224 that covers $112 \times 112(m^2)$ area around the ego-pose, at the present time. The map API enables access to the drivable area information around the spot where the dataset is collected. Based on the ego-pose, we query the drivable area and save the returned information into a binary mask that is assigned 1s at the pixels belonging to the drivable area, and 0s at the other pixels.

8.2 Argoverse Motion Forecasting Data

Argoverse motion forecasting [8] contains about 320,000 episodes, each of which spans 50 frames (5 seconds), along with a map API that gives an access to the drivable area information. All of the episodes are pre-processed for the trajectory forecasting task and, hence, additional extraction processes (such as association, smoothing, and imputation) are unnecessary. However, to condition the data samples to be as similar to the samples in the nuScenes trajectory (Section 8.1) as possible, we down-sample each episode to episode lengths of 10 frames (5 seconds). We also normalize the coordinate system, such that the ego-agent at

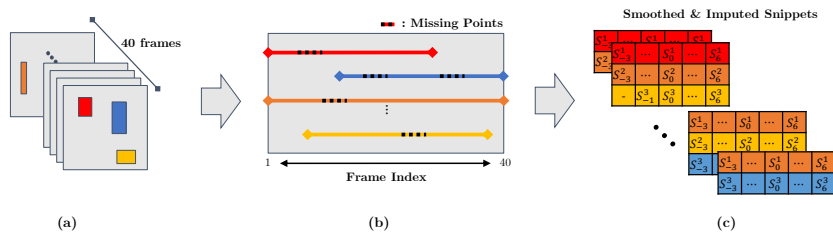


Fig. 8. Trajectory association, filtering and imputation process. (a), (b), (c) depict the bounding boxes in different frames, the associated and concatenated sequences, and the final trajectory snippets, respectively. Each agent is assigned a different color.

the present time is placed at the origin. As with nuScenes, we generate for each episode the road mask of dimension 224×224 which covers a $112 \times 112(m^2)$ area around the ego-agent at the present time.

8.3 Single-agent Forecasting Experiment With R2P2

Table 6. Single-agent Training results in NUSCENES.

Model	MINADE (\downarrow)	MINFDE (\downarrow)	Rf (\uparrow)	DAO (\uparrow)	DAC (\uparrow)
R2P2 (MSE) [26]	1.074	2.037	1.690	21.43	0.540
R2P2 (MAP)	0.877	1.591	2.624	24.17	0.541
CAM	1.320	2.708	1.000	3.13	0.549
CAM-NF	0.959	1.591	2.698	26.53	0.563
LOCAL-CAM-NF	0.786	1.419	2.567	22.69	0.542
GLOBAL-CAM-NF	0.782	1.412	2.633	22.90	0.542
ATTGLOBAL-CAM-NF	0.775	1.436	2.476	21.93	0.543

Since precise implementation details of R2P2-MA [27] are currently less known, our implementation of R2P2-MA based on the limited information makes unstable prediction outputs. Meanwhile, the implementation of the original R2P2 [26] model (for single-agent scenarios), which is well-introduced in the paper’s supplemental material and produces reasonable outputs. Therefore, we compare the original R2P2 model and with separate versions of our model—all of which are trained toward a single-agent prediction setting. In Table 6, R2P2 (MSE) is the original model in [26], R2P2 (MAP) is R2P2 trained with our new \tilde{p} introduced in the main paper, and others are as introduced in the main paper. In terms of all metrics, our models show better performance compared to R2P2 and R2P2 (MAP). We also highlight the fine-grained effect of using our differentiable drivable area map context: R2P2 (MAP) also outperforms the original R2P2 model in all metrics.

8.4 CARLA Trajectory Extraction Process and Experiments

CARLA [7] is a vehicle and pedestrian behavior simulator wherein the agents follow the physical laws of motions driven by Unreal Engine. In order to validate

the generalizability of our models, we synthesize trajectory forecasting data using CARLA vehicle Blueprints and record the trajectory for all simulation time-steps. We make sure the data format is consistent with that of Argoverse and nuScenes. The data extracted from the simulator includes: vehicle trajectories, 2D birds-eye-view map images, lane center-lines, and LiDAR point-cloud data. The physics engine (Unreal Engine 4.19) provides limited capability for producing actual surface contour points, with the provided in-built CARLA ray-tracing LiDAR sensor. Therefore, we utilize the depth image sensor to extract accurate depth information. We use four depth sensors, each with 90 deg field-of-view to capture depth images at each time-step. Then points are uniformly sampled on each image plane according to the number of channels and rotation frequency configuration of selected LiDAR. These points are corresponded with the pixel depth value by 2D bilinear interpolation and projected into 3D space. The points are assigned a distance and an azimuth angle and converted from spherical coordinate to Cartesian coordinate system. This simulates precise object-shape contoured LiDAR point-cloud. Additional map lane-center information is acquired from the map way-points, by minimizing hypotenuse distance at intersections.

In this paper, only birds-eye-view maps are used. These maps are utilized to build the distance transform of these images, as mentioned in Sec. 4.1 of the main paper. The drivable and non-drivable area information is extracted, based on the semantic segmentation of objects provided by the C++ API. The API is extended to specifically capture only the drivable area, and we utilize the Python API to capture as a binary road mask with respect to ego-vehicle in simulation-time.

As the calibration parameters are not provided by the Unreal Engine physics kit, the intrinsic and extrinsic camera parameters and the distortion parameters are estimated by multiple camera view bundle adjustment. These parameters are used to transform segmentation images from a perspective view to an orthographic birds-eye-view. The maps are synchronized with the trajectory data 20 points in the past trajectory segment and 30 points in the future trajectory segments for all agents in a snapshot. In each map, we fix the number of agents to 5, including the ego-vehicle. Engineered data can be further generated on similar lines, for specialized edge-case handling of model. We will release our extended CARLA dataset which presents multiple data modalities, corresponding simulation and data extraction codes for our fellow researchers.

Performance Analysis: Model generalizability depends on both the map characteristics as well as the statistical distribution of trajectory samples provided by the dataset. The CARLA dataset has simpler cases compared to the ones in ARGOVERSE. But there are scenic disturbances, like parked and moving agents in the private property-areas, which is considered as non-drivable area. Even considering these cases, the model is able to predict valid admissible trajectories, only influenced by the provided drivable area. We rigorously analyze the performance of our models in the CARLA dataset. The results are illustrated in Table 7 where our model outperforms in MINADE and MINFDE metrics by about 33% compared to baselines. CAM-NF model provides good performance in diversity metrics DAO and DAC illustrating NF capability in improving diversity. From the results, our proposed ATTGLOBAL-CAM-NF model is better

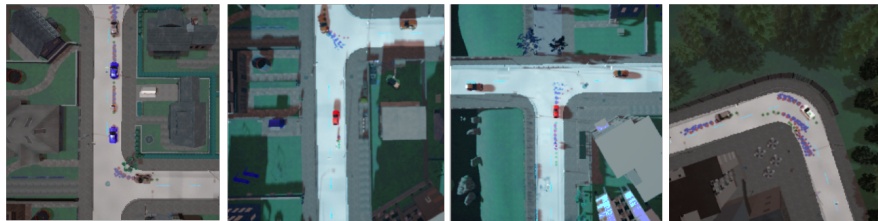


Fig. 9. Visualizing predictions over simulated CARLA dataset at a snapshot of simulation-time with birds-eye-view image of drivable and non-drivable area and map. The RED points indicate ground truth, GREEN points indicate past trajectory points and BLUE indicates future trajectory points

Table 7. Results of baseline models and our proposed model in CARLA dataset. LOCAL-CAM-NF is an ablation, whereas ATGLOBAL-CAM-NF is our full proposed model. The metrics are abbreviated as follows: MINADE(**A**), MINFDE(**B**), rF(**C**), DAO(**D**), DAC(**E**). Improvements indicated by arrows. *: larger is better, as long as **A** and **B** are small.

Model	CARLA				
	A (↓)	B (↓)	C (↑)*	D (↑)*	E (↑)*
LSTM	0.866	1.752	1.000	1.040	0.116
CSP [9]	0.671	1.271	1.000	0.990	0.112
MATF-D [39]	0.599	1.108	1.000	0.960	0.115
DESIRE [19]	0.712	1.228	1.767	0.339	0.169
MATF-GAN [39]	0.567	1.019	1.208	1.870	0.109
R2P2-MA [26]	0.660	1.114	1.899	4.963	0.111
CAM	0.695	1.421	1.000	0.950	0.143
CAM-NF	0.544	1.008	2.138	5.190	0.110
LOCAL-CAM-NF	0.486	0.881	2.236	4.930	0.110
GLOBAL-CAM-NF	0.493	0.902	2.143	4.780	0.111
ATGLOBAL-CAM-NF	0.461	0.865	2.041	4.290	0.113

able to mimic the true distribution of the autopilot in the simulator, showing considerable improvement in forecasting, over the baselines.

8.5 Analysis of α

We experiment with various values of α —a degradation coefficient of constant velocity. As shown in Table 8, models tend to perform better when trained with a certain range of α less than 1.0, reflecting that degrading the assumption of constant velocity (when $\alpha = 1.0$) prevents the model to avoid trivial solutions and encourages it to actively seek for necessary cues for predictions in non-constant velocity. Among values we experimented, we choose to set $\alpha = 0.5$ because both rF and DAO of the prediction show diverse and admissible while remaining competitive in MINERRORS and DAC, which is a desirable property in our case. A possible future direction of our degradation approach is to replace α with a learnable parametric function of noise centered at 1.0 that can perturb the physical model of the world, similarly discussed in [8].

Table 8. Analysis on α on NUSCENES.

Model	MINADE (\downarrow)	MINFDE (\downarrow)	rF (\uparrow)	DAO (\uparrow)	DAC (\uparrow)
ATTGLOBAL-CAM-NF(0.25)	0.699	1.230	2.457	12.10	0.401
ATTGLOBAL-CAM-NF(0.5)	0.688	1.251	2.477	12.28	0.399
ATTGLOBAL-CAM-NF(0.75)	0.664	1.245	2.428	11.89	0.399
ATTGLOBAL-CAM-NF(1.0)	0.840	1.680	1.972	11.85	0.397

9 Scene Context Processing

9.1 Differentiable Drivable Area Map and \tilde{p}

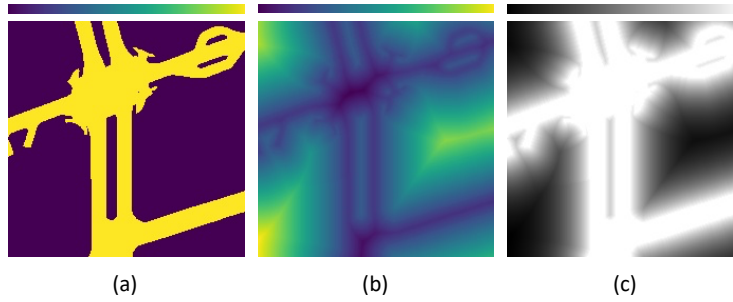


Fig. 10. (a) binary road mask, (b) differentiable drivable area, and (c) \tilde{p} in nuScenes. The colorbars indicate the scales of the pixel value (increasing from left to right).

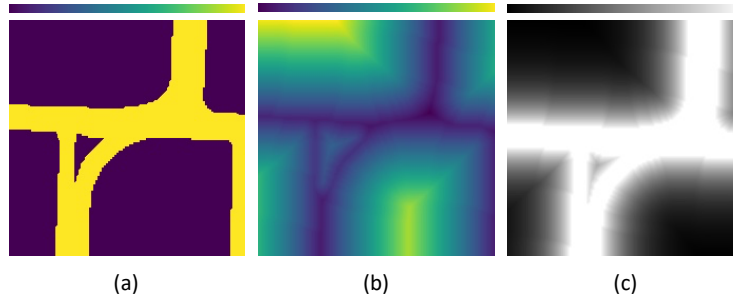


Fig. 11. (a) binary road mask, (b) differentiable drivable area, and (c) \tilde{p} in Argoverse. The colorbars indicate the scales of the pixel value (increasing from left to right).

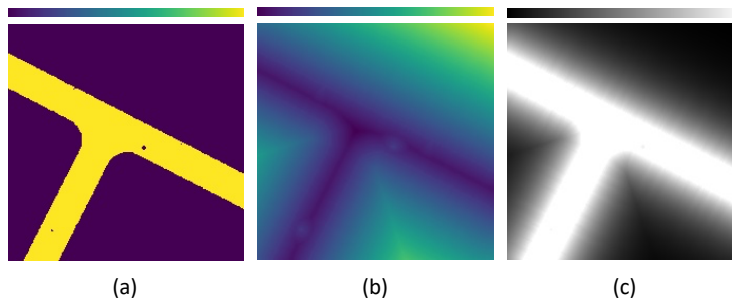


Fig. 12. (a) binary road mask, (b) differentiable drivable area, and (c) \tilde{p} in CARLA. The colorbars indicate the scales of the pixel value (increasing from left to right).

We utilize the 224×224 binary road masks in Sec. A.1 and Sec. A.2 to derive \tilde{p} , which is used in the evaluation of the reverse cross-entropy in our loss function at Eq. (9), the main paper. Since \tilde{p} is evaluated using 2×2 bilinear interpolation, the probability should be assigned to be gradually changing over the pixels, or the gradient would become 0 almost everywhere. To this end, we apply the distance transform to the binary mask, as depicted in Fig 10(b), Fig 11(b), Fig 12(b). We call this transformed map a *differentiable drivable area map* and utilize it for deriving \tilde{p} , as well as the scene context input Φ . As described in the main paper, our \tilde{p} is defined based on the assumptions that every location on the drivable-area is equally probable for future trajectories to appear in and that the locations on non-drivable area are increasingly less probable, proportional to the distance from the drivable area. Hence, we first set the negative-valued pixels (drivable region) in a differentiable drivable area map to have 0s assigned and subtract each pixel from the maximum-value so that the pixel values in the drivable-area are uniformly greatest over the map. Then, we normalize the map with the mean and standard deviation calculated over the training dataset to smooth the deviations. Finally, we apply softmax over the pixels to constitute the map as a probability distribution \tilde{p} , as depicted in Fig 10(c), Fig 11(c), Fig 12(c).

9.2 Generating scene context input Φ

The scene context input $\Phi \in \mathbb{R}^{224 \times 224 \times 3}$ is directly generated utilizing the differentiable drivable area map. We augment 2 extra channels to the map, which embeds the unique pixel indices and Euclidean distances between each pixel and the center of the map. This way the ConvNet is enabled the access to the spatial position in the input thus it can extract the location-specific features from the scene context input. As similarly to the \tilde{p} , we normalize this augmented with the mean and standard deviation calculated over the training dataset to smooth the deviations.

10 Additional Results Visualization

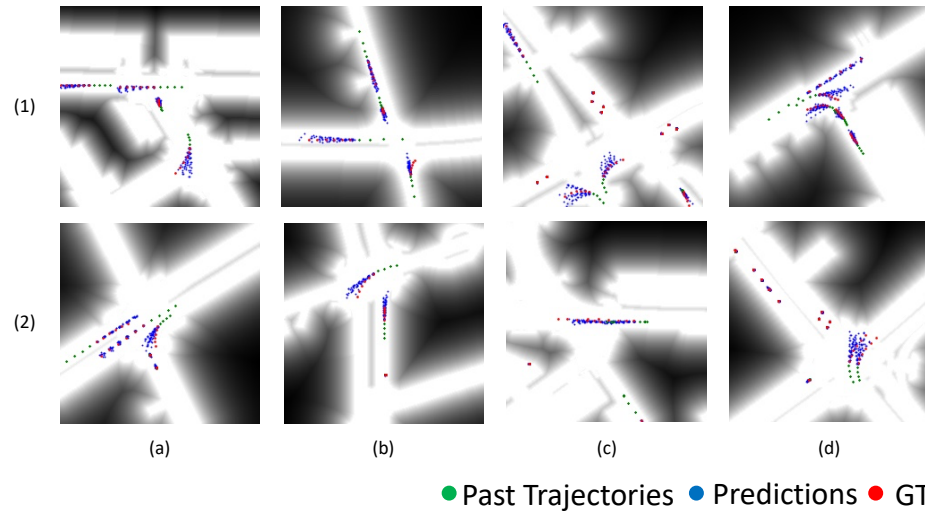


Fig. 13. Prediction results on nuScenes. Brighter background colors represent greater \bar{p} values. Our approach predicts future trajectories that show diversity while remaining admissible.

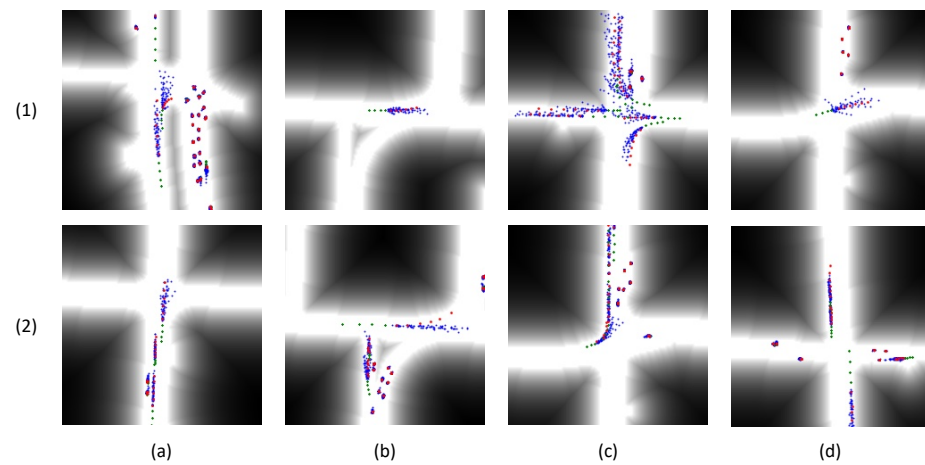


Fig. 14. Prediction results on Argoverse. Brighter background colors represent greater \bar{p} values. Our approach predicts future trajectories that show diversity while remaining admissible.

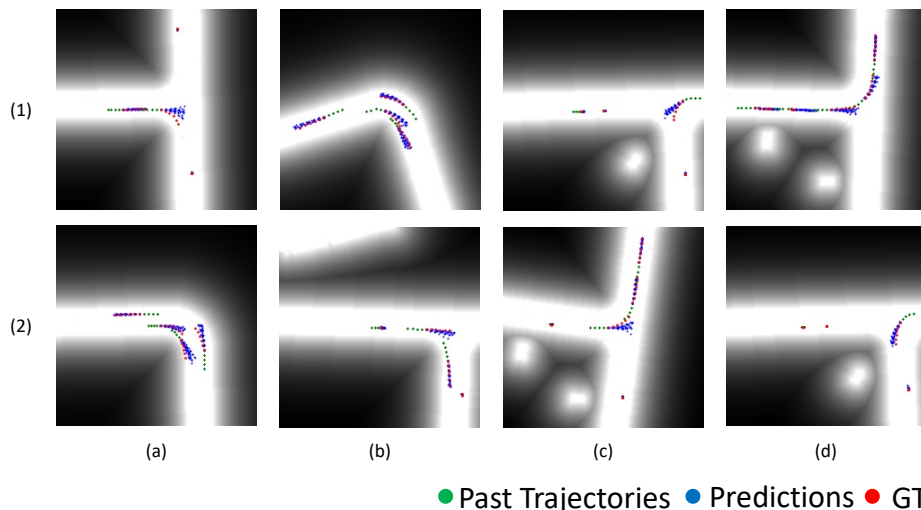


Fig. 15. Prediction results on CARLA. Brighter background colors represent greater \hat{p} values. Our approach predicts future trajectories that show diversity while remaining admissible.

Prediction results on nuScenes, Argoverse, and CARLA are illustrated in Fig 13, Fig 14, and Fig 15, respectively. In most cases throughout all three datasets, our model shows diverse and admissible predictions, even in the case of rapid left or right turns as in (2)(d) in Fig 13 and (1)(d) and (2)(d) in Fig 15. An clear insight on the quality of our model can be noticed when comparing predictions in cases of one path and multiple paths in front. For example, cases in (1)(b) and (2)(c) in Fig 13 show predictions are mostly going forward given the scene and the past trajectories going forward, whereas cases in (1)(c) and (2)(d) in Fig 13 show predictions are diverse given the shape of the road and the past trajectories that start to make turns. One weakness of our experimental setting is that it is quite challenging for our model to predict an explicit left or right turn given the past trajectory going only forward as illustrated in the bottom-most trajectory in (1)(b) in Fig 13 and (1)(a) in Fig 15. One possible feature that can be added to avoid such cases would be to incorporate encoded lane information in our cross-agent interaction module along with trajectory encodings.

11 Architecture and Training Details

11.1 Training Setup

For all experiments, we implemented models using the PyTorch 1.3.1 framework. We performed all data extraction and model training on a desktop machine with a NVIDIA TITAN X GPU card. We directly utilized the default implementations of Adam optimizer [16] with the initial learning rate of 1.0E-04 and an adaptive scheduler that halves the learning rate with patience parameter 3 based on the sum of the AVGADE and AVGFDE in validation. The batch size is 64 for all baselines and the proposed model except ATTGLOBAL-CAM-NF, where the batch size of 4 is used. We train the model for maximum 100 epochs, however, the early stopping is applied when the over-fitting of a model is observed.

Table 9. Network Hyperparameters.

Operation	Input (dim.)	Output (dim.)	Parameters
CONVNET			
(Every Conv2D is with ‘same’ padding, and followed by BN [9] & ReLU.)			
<i>Conv2D</i>	Φ (64, 64, 3)	<i>conv1</i> (64, 64, 16)	kernel:=(3,3)
<i>Conv2D</i>	<i>conv1</i>	<i>conv2</i> (64, 64, 16)	kernel:=(3,3)
<i>MaxPool2D</i>	<i>conv2</i>	<i>pool2</i> (32, 32, 16)	kernel:=(2,2), stride:=(2,2)
<i>Conv2D</i>	<i>pool2</i>	<i>conv3</i> (32, 32, 32)	kernel:=(5,5)
<i>Conv2D</i>	<i>conv3</i>	<i>conv4</i> (32, 32, 6)	kernel:=(1,1)
<i>Dropout</i>	<i>conv3</i>	Γ_g (32, 32, 32)	p:=0.5
<i>UpSample2D</i>	<i>conv4</i>	Γ_l (100, 100, 6)	mode:=bilinear
TRAJECTORY ENCODING MODULE			
(Repeated for $a \in \{1, 2, \dots, A\}$ with variable encoding time length $T_{past}^a := t_s^a + 1$)			
<i>Difference</i>	$S_{past}^a (T^a, 2)$	$dS_{past}^a (T^a, 2)$	zero-pad (at the <i>start time</i>)
<i>Fully-connected</i>	dS_{past}^a	$tS_t^a (T^a, 128)$	activation:=Linear
<i>LSTM</i>	tS_t^a	h_0^a (128)	zero initial states
CROSS-AGENT INTERACTION MODULE			
(Repeated for $a \in \{1, 2, \dots, A\}$)			
<i>LayerNorm</i>	h_0^a (128)	h_n^a (128)	Layer Normalization [2]
<i>Fully-connected</i>	$h_{in}^a \forall a \in \{1, 2, \dots, A\}$	\mathbf{Q} (A, 128)	activation:=Linear
<i>Fully-connected</i>	$h_{in}^a \forall a \in \{1, 2, \dots, A\}$	\mathbf{K} (A, 128)	activation:=Linear
<i>Fully-connected</i>	$h_{in}^a \forall a \in \{1, 2, \dots, A\}$	\mathbf{V} (A, 128)	activation:=Linear
<i>Attention</i>	$\mathbf{Q}, \mathbf{K}, \mathbf{V}$	h_{atn}^a (128)	Scaled dot-product attention
<i>Addition</i>	h_0^a, h_{atn}^a	\tilde{h}^a (128)	$\tilde{h}^a = h_0^a + h_{atn}^a$
LOCAL SCENE EXTRACTOR			
(Repeated for $a \in \{1, 2, \dots, A\}$)			
<i>Bilinear</i>	$\Gamma_l, \hat{S}_{t-1}^a$ (2)	γ_t^a (6)	2×2 Bilinear Interpolation
<i>Concatenate</i>	\tilde{h}^a, γ_t^a	hg_t^a (134)	-
<i>Fully-connected</i>	hg_t^a	fhg_t^a (50)	activation:=Softplus
<i>Fully-connected</i>	fhg_t^a	lc_t^a (50)	activation:=Softplus
AGENT-TO-SCENE INTERACTION MODULE			
(Repeated for $a \in \{1, 2, \dots, A\}$ with the fixed decoding time length 6)			
<i>Flatten</i>	$\hat{S}_{0:t-1}^a (t, 2)$	$f\hat{S}_{0:t-1}^a$ (12)	zero-pad (at the last), $\hat{S}_0^a := S_0^a$
<i>GRU</i>	$f\hat{S}_{0:t-1}^a$	\tilde{h}_t^a (150)	zero initial state
<i>Fully-connected</i>	\tilde{h}_t^a	fh_t^a (150)	activation:=Linear
<i>Fully-connected</i>	Γ_g	$f\Gamma$ (32, 32, 150)	activation:=Linear
<i>Attention</i>	$fh_t^a, f\Gamma$	$\alpha\Gamma_t^a$ (32, 32, 1)	Additive attention
<i>Pool</i>	$\Gamma_g, \alpha\Gamma_t^a$	$\tilde{\gamma}_t^a$ (32)	Pixel-wise sum ($\Gamma_g \odot \alpha\Gamma_t^a$)
<i>Concatenate</i>	$\tilde{\gamma}_t^a, \tilde{h}_t^a, lc_t^a$	gc_t^a (232)	-
FLOW DECODER			
(Repeated for $a \in \{1, 2, \dots, A\}$)			
<i>Fully-connected</i>	gc_t^a	fjc_t^a (50)	activation:=Softplus
<i>Fully-connected</i>	fjc_t^a	$ffjc_t^a$ (50)	activation:=Tanh
<i>Fully-connected</i>	$ffjc_t^a$	\hat{u}_t^a (2), $\hat{\sigma}_t^a$ (2, 2)	activation:=Linear
<i>Expn</i>	$\hat{\sigma}_t^a$	σ_t^a (2, 2)	impl. in [4]
<i>Constraint</i>	$\hat{\mu}_t^a, \hat{S}_{t-2:t-1}^a$	μ_t^a (2)	$\alpha := 0.5$
<i>Random.</i>	-	z_t^a (2)	$z_t^a \sim \mathcal{N}(0, I)$
<i>Transform</i>	$z_t^a, \mu_t^a, \sigma_t^a$	S_t^a (2)	$S_t^a = \sigma_t^a z_t^a + \mu_t^a$

11.2 Hyperparameters

Our experiments involve predicting 3 seconds of future trajectories of surrounding agents given a past record of 2 seconds, that includes the past trajectories and the scene context at the present time. The setting is common over all three datasets (nuScenes [6], Argoverse [8], and CARLA [7]) that we experiment. The trajectories are represented as 2D position sequences recorded at every 0.5 seconds. The hyperparameters of the network structure is described in Table 9 and Sec. 11.3.

11.3 Network Details

In this section, we discuss the details on the network architecture of our model, which are not discussed in the main paper. The details of the the cross-agent attention and the agent-to-scene attention are particularly included in the discussion. We also give the edge case (e.g., bilinear interpolation at the position out of scene range) handling methods in our model. Refer to Table 9 for the hyperparameters used in the components of our model.

We first discuss the details in the *encoder*. As described in the main paper, the encoder is made of the trajectory encoding module and cross-agent interaction module. The trajectory encoding module utilizes a linear transform and a single layer LSTM to encode the observation trajectory for each agent $S_{past}^a \equiv S_{t_s^a:0}^a$. To encode the observation trajectory S_{past}^a , we first normalize it to dS_{past}^a by taking the differences between the positions at each time step to have a translation-robust representation. Then, we linearly transform the normalized sequence dS_t^a to a high dimensional vector tS_t^a with Eq. (13) then the vector is fed to the LSTM with Eq. (14) to update the state output h_t^a and the cell state c_t^a of the LSTM.

$$tS_t^a = \text{LINEAR}_1(dS_t^a) \quad (13)$$

$$h_{t+1}^a, c_{t+1}^a = \text{LSTM}(tS_t^a, h_t^a, c_t^a) \quad (14)$$

Wrapping Eq. (13) and Eq. (14), along with the trajectory normalization process into a single function, we get Eq. (1) in the main paper, where the same equation is copied as Eq. (15) for the convenience. Note that the initial states of the LSTM are set as zero-vectors.

$$h_{t+1}^a = \text{RNN}_1(S_t^a, h_t^a) \quad (15)$$

The cross-agent interaction module gets the set of agent embeddings $\mathbf{h}_0 = \{h_0^1, \dots, h_0^A\}$ and models the agent-to-agent interaction via an attention architecture inspired by “self-attention” [35]. For each agent encoding h_0^a , we first apply *Layer Normalization* [2] to get the normalized representation h_{ln}^a in Eq. (16) and calculate the query-key-value triple (Q^a, K^a, V^a) by linearly transforming h_{ln}^a with Eq. (17)-(19). Note that we empirically found that Layer Normalization gives a slight improvement to the model performance.

$$h_{ln}^a = \text{LAYERNORM}(h_0^a) \quad (16)$$

$$Q^a = \text{LINEAR}_Q(h_{ln}^a) \quad (17)$$

$$K^a = \text{LINEAR}_K(h_{ln}^a) \quad (18)$$

$$V^a = \text{LINEAR}_V(h_{ln}^a) \quad (19)$$

Next, we calculate the attention weights $\mathbf{w}^a \equiv \{w_1^a, w_2^a, \dots, w_A^a\}$ by calculating *scaled dot-product* between the query Q^a and each key in the set of keys $\mathbf{K} \equiv \{K^1, K^2, \dots, K^A\}$ with Eq. 20 and taking softmax over the set of products with Eq. 21.

$$\text{SD}_{a,a'} = \frac{Q^a \cdot K^{a'}}{\sqrt{\dim(Q^a)}} \quad (20)$$

$$\mathbf{w}^a = \text{SOFTMAX}(\{\text{SD}_{a,1}, \text{SD}_{a,2}, \dots, \text{SD}_{a,A}\}) \quad (21)$$

Finally, we get the interaction feature $\text{ATTENTION}_1(Q^a, \mathbf{K}, \mathbf{V})$ in Eq. (2) in the main paper, by taking the weighted average over $\mathbf{V} \equiv \{V^1, V^2, \dots, V^A\}$ using the weights \mathbf{w}^a with Eq. (22).

$$\text{ATTENTION}_1(Q^a, \mathbf{K}, \mathbf{V}) = \sum_{a'=1}^A w_{a'}^a V^{a'} = h_{atn}^a \quad (22)$$

We now discuss the details in *decoder*. As described in the main paper, the decoder is autoregressively defined and the previous outputs $\hat{S}_{0:t-1}^a$ are fed back. We encode the previous outputs using a GRU. Since the GRU requires a static shaped input at each time step, we reconfigure $\hat{S}_{0:t-1}^a$ by flattening and zero-padding it with Eq. (23) and the reconfigured vector $f\hat{S}_{0:t-1}^a$ is fed to the GRU at each decoding step with Eq. (24).

$$f\hat{S}_{0:t-1}^a = \{\text{FLATTEN}(\hat{S}_{1:t-1}^a), 0, \dots, 0\} \quad (23)$$

$$\hat{h}_t^a = \text{GRU}(f\hat{S}_{0:t-1}^a, \hat{h}_{t-1}^a) \quad (24)$$

Wrapping Eq. (23) and Eq. (24) to a single function, we get Eq. (3) in the main paper, where the same equation is copied as Eq. 25 for the convenience. Note that the initial state of the GRU is set as a zero-vector.

$$\hat{h}_t^a = \text{RNN}_2(\hat{S}_{1:t-1}^a, \hat{h}_{t-1}^a) \quad (25)$$

The encoding \hat{h}_t^a at each step is utilized in the agent-to-scene interaction module. The module is designed with an attention architecture inspired by “visual-attention” [38]. We first linearly transform \hat{h}_t^a and each pixel Γ_g^i in the scene feature $\mathbf{\Gamma}_g \equiv \{\Gamma_g^1, \Gamma_g^2, \dots, \Gamma_g^{HW}\}$ with Eq (26),(27).

$$fh_t^a = \text{LINEAR}_{\hat{h}}(\hat{h}_t^a) \quad (26)$$

$$f\Gamma^i = \text{LINEAR}_{\Gamma_g}(\Gamma_g^i) \quad (27)$$

Then, we calculate the additive attention $\text{ATTENTION}_2(\hat{h}_t^a, \mathbf{\Gamma})$ in Eq. (4) of the main paper by taking the addition of fh_t^a to each $f\Gamma^i$ followed by ReLU in Eq. (28), then applying softmax with Eq. (29).

$$\text{SR}_{a,i} = \text{RELU}(fh_t^a + f\Gamma^i) \quad (28)$$

$$\text{ATTENTION}_2(\hat{h}_t^a, \mathbf{\Gamma}) = \text{SOFTMAX}(\{\text{SR}_{a,1}, \text{SR}_{a,2}, \dots, \text{SR}_{a,HW}\}) = \alpha \mathbf{\Gamma}_t^a \quad (29)$$

Further details on our model’s architecture and the hyperparameters, for instance the ConvNet and fully-connected layers discussed in the main paper are listed and defined in Table 9.

References

1. Abbeel, P.: Maximum likelihood (ml), expectation maximization (em). Course Note (2011), https://people.eecs.berkeley.edu/~pabbeel/cs287-fa11/slides/Likelihood_EM_HMM_Kalman-v2.pdf
2. Ba, J.L., Kiros, J.R., Hinton, G.E.: Layer normalization. arXiv preprint arXiv:1607.06450 (2016)
3. Bernstein, D.S., So, W.: Some explicit formulas for the matrix exponential. *IEEE Transactions on Automatic Control* **38**(8), 1228–1232 (1993)
4. Caesar, H., Bankiti, V., Lang, A.H., Vora, S., Liong, V.E., Xu, Q., Krishnan, A., Pan, Y., Baldan, G., Beijbom, O.: nuscenes: A multimodal dataset for autonomous driving. arXiv preprint arXiv:1903.11027 (2019)
5. Chang, M.F., Lambert, J., Sangkloy, P., Singh, J., Bak, S., Hartnett, A., Wang, D., Carr, P., Lucey, S., Ramanan, D., et al.: Argoverse: 3d tracking and forecasting with rich maps. In: *Proceedings of the IEEE Conference on Computer Vision and Pattern Recognition*. pp. 8748–8757 (2019)
6. Deo, N., Trivedi, M.M.: Convolutional social pooling for vehicle trajectory prediction. In: *Proceedings of the IEEE Conference on Computer Vision and Pattern Recognition Workshops*. pp. 1468–1476 (2018)
7. Dosovitskiy, A., Ros, G., Codevilla, F., Lopez, A., Koltun, V.: Carla: An open urban driving simulator. arXiv 2017. arXiv preprint arXiv:1711.03938
8. Fortunato, M., Azar, M.G., Piot, B., Menick, J., Osband, I., Graves, A., Mnih, V., Munos, R., Hassabis, D., Pietquin, O., et al.: Noisy networks for exploration. arXiv preprint arXiv:1706.10295 (2017)
9. Ioffe, S., Szegedy, C.: Batch normalization: Accelerating deep network training by reducing internal covariate shift. arXiv preprint arXiv:1502.03167 (2015)
10. Kingma, D.P., Ba, J.: Adam: A method for stochastic optimization. arXiv preprint arXiv:1412.6980 (2014)
11. Lee, N., Choi, W., Vernaza, P., Choy, C.B., Torr, P.H., Chandraker, M.: Desire: Distant future prediction in dynamic scenes with interacting agents. In: *Proceedings of the IEEE Conference on Computer Vision and Pattern Recognition*. pp. 336–345 (2017)
12. Rhinehart, N., Kitani, K.M., Vernaza, P.: R2p2: A reparameterized pushforward policy for diverse, precise generative path forecasting. In: *Proceedings of the European Conference on Computer Vision (ECCV)*. pp. 772–788 (2018)
13. Rhinehart, N., McAllister, R., Kitani, K., Levine, S.: Precog: Prediction conditioned on goals in visual multi-agent settings. In: *Proceedings of the IEEE International Conference on Computer Vision*. pp. 2821–2830 (2019)
14. Vaswani, A., Shazeer, N., Parmar, N., Uszkoreit, J., Jones, L., Gomez, A.N., Kaiser, L., Polosukhin, I.: Attention is all you need. In: *Advances in neural information processing systems*. pp. 5998–6008 (2017)
15. Xu, K., Ba, J., Kiros, R., Cho, K., Courville, A., Salakhudinov, R., Zemel, R., Bengio, Y.: Show, attend and tell: Neural image caption generation with visual attention. In: *International conference on machine learning*. pp. 2048–2057 (2015)
16. Yu, B.M., Shenoy, K.V., Sahani, M.: Derivation of kalman filtering and smoothing equations. Course Note (2004), http://users.ece.cmu.edu/~byronyu/papers/derive_ks.pdf

17. Zhao, T., Xu, Y., Monfort, M., Choi, W., Baker, C., Zhao, Y., Wang, Y., Wu, Y.N.: Multi-agent tensor fusion for contextual trajectory prediction. In: Proceedings of the IEEE Conference on Computer Vision and Pattern Recognition. pp. 12126–12134 (2019)